PROCEEDINGS OF SPIE

SPIEDigitalLibrary.org/conference-proceedings-of-spie

Space object identification using phase-diverse speckle

John H. Seldin, Michael F. Reiley, Richard G. Paxman, Bruce E. Stribling, Brent L. Ellerbroek, et al.

John H. Seldin, Michael F. Reiley, Richard G. Paxman, Bruce E. Stribling, Brent L. Ellerbroek, Dustin C. Johnston, "Space object identification using phase-diverse speckle," Proc. SPIE 3170, Image Reconstruction and Restoration II, (31 October 1997); doi: 10.1117/12.292817

SPIE.

Event: Optical Science, Engineering and Instrumentation '97, 1997, San Diego, CA, United States

Invited Paper

Space-object identification using phase-diverse speckle

John H. Seldin, Michael F. Reiley and Richard G. Paxman
Advanced Information Systems Group
ERIM International
P.O. Box 134008, Ann Arbor, Michigan 48113-4008
(313) 994-1200 ext. 2361; email: seldin@erim.org

Bruce E. Stribling
Air Force Maui Optical Station
535 Lipoa Parkway. Suite 200
Kihei, HI 96753
(808) 875-8390 email: bstribli@falcon.mhpcc.af.mil

Brent L. Ellerbroek and Dustin C. Johnston
Starfire Optical Range
U.S. Air Force Phillips Laboratory
Kirtland Air Force Base
New Mexico 87117-5776
(505) 846-4712 ext. 364; email: ellerbrb@plk.af.mil

ABSTRACT

Space-object identification from ground-based telescopes is challenging because of the degradation in resolution arising from atmospheric turbulence. Phase-diverse speckle is a novel post-detection correction method that can be used to overcome turbulence-induced aberrations for telescopes with or without adaptive optics. We present a simulation study of phase-diverse speckle satellite reconstructions for the Air Force Maui Optical Station 1.6-meter telescope. For a given turbulence strength, satellite reconstruction fidelity is evaluated as a function of quality and quantity of data. The credibility of this study is enhanced by reconstructions from actual compensated data collected with the 1.5-meter telescope at the Starfire Optical Range. Consistent details observed across a time series of reconstructions from a portion of a satellite pass enhance the authenticity of these features. We conclude that phase-diverse speckle can restore fine-resolution features not apparent in the raw aberrated images of space objects.

Keywords: image reconstruction, phase diversity, phase-diverse speckle, space-object identification

SPIE Vol. 3170 • 0277-786X/97/$10.00

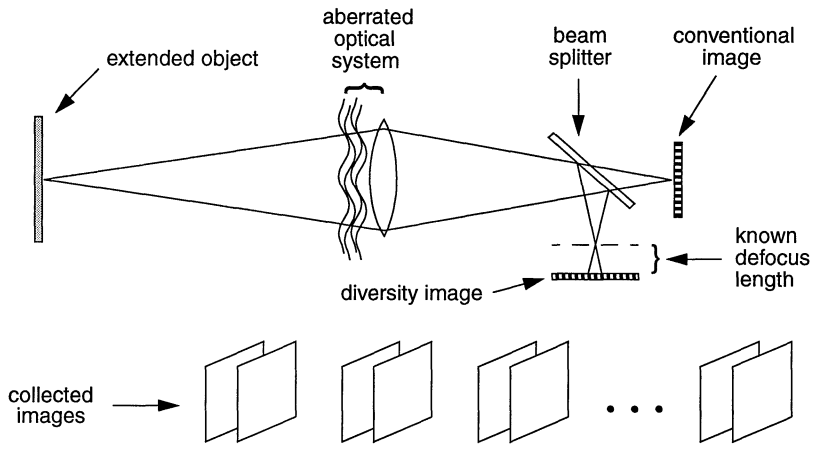

Figure 1: Phase-diverse speckle data-collection scheme.

1. INTRODUCTION

With its three optical platforms, including a 1.6-meter telescope, the Air Force Maui Optical Station (AMOS) serves as a source of fine-resolution ground-based space-object imagery. One of the goals of AMOS is to provide the highest quality imagery possible in a timely manner for further analysis, interpretation, and identification of these objects. The resolution achieved in space-object imaging is usually limited by turbulence-induced aberrations, which can severely limit the resolution in the images by an order of magnitude or more. Until recently, the 1.6-meter telescope relied upon an adaptive-optics system to eliminate in real time much of the phase aberrations introduced by atmospheric turbulence. However, this system was recently decommissioned, so post-collection methods for restoring the spatial resolution lost to the effects of turbulence are more important than ever. Even when an adaptive-optics system is available, the correction is never perfect. There are several sources of residual aberrations that degrade the imagery: imperfect wavefront sensing (particularly in low light-level situations), the time lag between sensing and correction (which allows for evolution of the atmosphere and is a particular problem when slewing to track an earth-orbiting space object), and deformable-mirror fitting errors. There are also scenarios in which adaptive-optics compensation is intermittent, degraded, or simply unavailable. A post-detection image-reconstruction capability also insures the continuing availability of fine-resolution images, even during adaptive-optics down time owing to routine maintenance or temporary system failure. Therefore, post-detection reconstruction methods provide an important complement to and backup for pre-detection correction.

Having motivated the need for post-detection image restoration, we now introduce the collection and reconstruction technique investigated here. The value of short-exposure data was first recognized by Labeyrie [1], who noticed that short-exposure images contain spatial-frequency information out to the diffraction-limited cutoff frequency. There are a variety of methods that have been developed over the years that take advantage of this observation, including speckle imaging [1, 2] and deconvolution from wavefront sensing [3, 4]. Among the more recent approaches that utilize an estimation-theoretic framework is a novel data-collection and post-detection processing technique called *Phase-Diverse Speckle* (PDS) [5, 6, 7, 8]. A schematic of the PDS collection modality is shown in Figure 1. PDS blends the strengths of short-exposure speckle data and phase-diversity imaging. In phase-diversity imaging [9, 10, 11], two or more images are simultaneously collected – a conventional image that is degraded by unknown aberrations and a second

(diversity) image that is intentionally defocused by a known amount. PDS data are recorded when a pair of short-exposure images (conventional and diversity) are collected for each of multiple realizations of aberration. PDS has been demonstrated on solar astronomy data [7, 8, 12] and on adaptive-optics compensated images of binary stars [13] collected with the 1.5-meter telescope at the Air Force Phillips Laboratory Starfire Optical Range (SOR).

The derivation of the PDS reconstruction algorithm will only be summarized here, and we refer the reader to the open literature cited above for the details of the estimation-theoretic framework employed. A detailed imaging model is constructed, and the noise characteristics of the collected data are used to establish the probability of measuring a set of images given a particular object and set of aberrations. This probability function is reinterpreted to express a complementary function of the object and aberrations that describes the likelihood that a given set of data were derived from these quantities. The restored object and the ensemble of unknown aberrations are obtained by maximizing the log of this function with respect to parameters describing the object and aberrations. A closed-form expression for the maximum of the log-likelihood function is not available, and so an iterative optimization procedure is required to search for the parameters that maximize the function. Closed-form expressions for the gradient enable us to use gradient-based techniques to optimize the log-likelihood function with respect to the large number of unknown parameters. Parameterization strategies include Zernike polynomials for describing aberrations associated with atmospheric turbulence [14] and the method of sieves for describing the object as the superposition of weighted resolution kernels [7, 15]. These strategies become more important for regularizing the estimates as the data from which they are derived become more corrupted by noise.

We begin by discussing a simulation study of PDS satellite reconstructions for the AMOS 1.6-meter telescope. For a given turbulence strength, satellite reconstruction fidelity is evaluated as a function of noise in the data and the number of phase-diverse pairs utilized. The credibility of the results of this study is enhanced by the reconstructions from real data collected with adaptive-optics compensation using the 1.5-meter telescope at the SOR. Excellent reconstructions are obtained using as few as 8 image pairs. In addition, consistent details observed across a time series of reconstructions from a portion of a satellite pass enhance the authenticity of the individual members of the sequence. The findings presented herein provide convincing evidence of the ability of PDS to restore fine-resolution details not found in aberrated images of space objects.

2. AMOS SIMULATION STUDY

A set of 64 random phase aberration realizations with Kolmogorov statistics and a satellite rendering were combined to form an ensemble of simulated, short-exposure, phase-diverse image pairs. The phase aberrations were used to make Nyquist-sampled point-spread functions (PSF's) at a wavelength of $0.7\mu m$ for both a conventional (in-focus) image channel and a diversity channel with 0.7 wave quadratic peak-to-valley defocus phase error. The phase aberrations were generated to match those encountered by the 1.6-meter AMOS telescope, and are parameterized by Fried's seeing parameter, r_0, which is typically 10 cm (at $\lambda = 0.5\mu m$) or less at the AMOS site. We present results for $r_0 = 10$ cm here.

The PSF's were convolved with the satellite rendering to generate noiseless images. The noiseless imagery must then be corrupted with signal-dependent noise and detector noise. The signal-dependent noise is a Poisson noise process that is independent of other detector noise sources. Visual magnitude, m_v, is a common parameter for specifying the photon flux of astronomical objects at the surface of the earth [16]. Using a fractional optical bandwidth, $\Delta\lambda/\lambda$, of 10% and an overall transmittance efficiency of 0.5 for whatever medium and/or optical system the light propagates through, a zero-magnitude object provides a photon flux of 0.3414×10^{10} $photons/(m^2 sec)$ at the surface of the earth at a wavelength of $0.7\mu m$. From these assumptions, the photon flux was calculated for the cases of m_v=4, 5, 6, and 7 and an exposure

time of 16 *msec*. This is a commonly used exposure time for the AMOS system, and objects with m_v in the range of 4 to 7 are typically encountered in operations. To incorporate detector characteristics, mean dark-current and flat-field maps estimated from the MIT Lincoln Laboratory CCD used at AMOS were incorporated. The flat-field, $\eta_k(x)$, in image channel k is a function of pixel location, x, and represents the non-uniform gain typically associated with a CCD detector array. The mean dark charge, $b_k^d(x;\tau)$, is an additive, Poisson noise source that is a function of exposure time, τ. To form the noise-corrupted images, each noiseless image was multiplied by the flat and the result was added to $b_k^d(x;\tau)$. At this point, each image was corrupted with Poisson noise. This was followed by the addition to each pixel of an additive Gaussian noise component (independent from pixel to pixel) with a standard deviation, σ_r. The readout noise for the AMOS CCD has been estimated as $\sigma_r = 9.1$ electrons. The seeds used to generate the random noise processes on the computer were varied from noise source to noise source and from image to image to simulate the independence of the noise across the large number of images.

Ensemble Image SNR

To calibrate visual magnitude in more familiar terms, we seek to define the signal-to-noise ratio (SNR) of the simulated imagery. The calculation of the SNR for an image of an object with compact support (like a satellite) is complicated by a number of considerations. First, the SNR is different at each pixel in the image due to the signal-dependent nature of the image and dark-current photon noise. Second, even if we know the compact support of the satellite, some definition of support is still required for a blurred image of the object. Because the blurring function extends to infinity, the support of the blurred object does as well. If we want to be able to say something useful about the SNR of an aberrated image (even on a pixel-by-pixel basis), then we need to define a support for that image that is finite. The fact that the blurring varies with aberration realization means that a new support could be defined for every image.

We seek a definition that enables us to distill the signal-to-noise levels to a single number that represents the SNR for a *set* of data collected in an image channel. This alleviates the need to report the SNR on a per-image or even a per-pixel-per-image basis. This SNR figure would be a single, representative number for the entire set of images that provides a useful measure of the strength of the signal with respect to the noise level at a typical point in a typical image. We begin by defining the SNR of a pixel at location x for realization j of an image in channel k as

$$\mathcal{S}_{jk}(x) = \frac{\eta_k(x) g_{jk}(x)}{[\eta_k(x) g_{jk}(x) + b_k^d(x;\tau) + \sigma_r^2]^{\frac{1}{2}}} , \tag{1}$$

where $g_{jk}(x)$ is the noiseless, aberrated image and $\eta_k(x) g_{jk}(x)$ incorporates the pixel-by-pixel CCD responsivity. Eq. (1) defines the SNR as the ratio of the expected value of the signal to the standard deviation due to three, independent noise sources: signal-dependent, dark-current, and CCD-readout noise.

To compress the pixel-by-pixel SNR defined in Eq. (1) into a single number, we define a SNR in channel k for an ensemble of J images collected in the channel. We begin by forming a "shift-and-add" image, defined as

$$\bar{d}_k(x) = \frac{1}{J} \sum_{j=1}^{J} [d_{jk}(x - x_j^r) - b_k^d(x - x_j^r;\tau)] , \tag{2}$$

where x_j^r is a shift to the nearest pixel that brings the jk^{th} detected image, $d_{jk}(x)$, into registration with the other $J-1$ images in the ensemble. To find x_j^r, we define an arbitrary reference image to which the other $J-1$ images are aligned; that is, $x_j^r = 0$ for one value of j. We normally select the image that is centered the best within the field of view (FOV). Note that the image shift from realization to realization is the

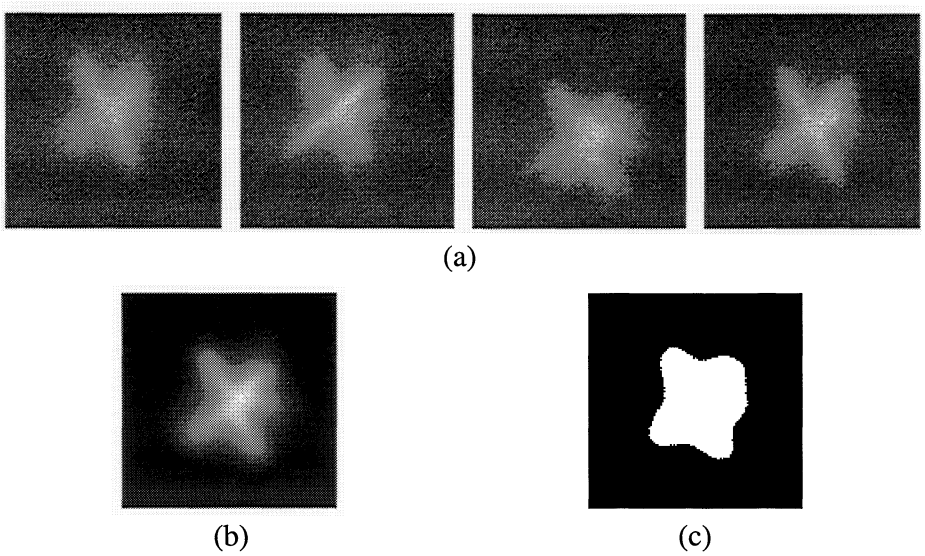

Figure 2: Support estimate for SNR calculation. (a) Examples of simulated focal-plane ($k = 1$) images for a satellite with $m_v = 5$; (b) Shift-and-add image, $\bar{d}_1$, formed from $J = 64$ images; (c) Support, $\Omega_1(0.8)$, obtained by thresholding (b) at the value for which 80% of the total energy is stored in pixels with intensities exceeding this threshold.

same for each image channel, so x_j^r is independent of k. In practice, we use the focal-plane image channel ($k = 1$ by convention), and we estimate x_j^r from the location of the maximum of the cross-correlation of the bias-corrected $d_{j1}(x)$ [as in the summand in Eq. (2)] with the reference image. There are two advantages to using the shift-and-add image to define the ensemble SNR. First, $\bar{d}_k(x)$ is formed through an averaging process that provides a better estimate of the mean signal at a typical pixel. Second, the support of $\bar{d}_k$ is easier to define than the support of an individual image from the ensemble.

A SNR metric that averages over pixels collected in the sensor FOV can depend on the ratio of the nominal size of the image to the size of the FOV. In the case of compact objects, we want to limit the contribution to the SNR estimate to those pixels that lie on or very near to the image of the object. Pixels far from the relatively compact image would have a very low SNR, and would pull down the average SNR if the image does not fill the entire FOV. Thus, our strategy is to define a support for the shift-and-add image over which we calculate the SNR. We define the support as a function of a single parameter, v:

$$\Omega_k(v) \;=\; \{x:\; \bar{d}_k(x) \;>\; T_k(v)\}\;,\quad 0 < v < 1 \tag{3}$$

where $T_k(v)$ is a threshold for which the following equation is satisfied:

$$\sum_{x \in \Omega_k(v)} \bar{d}_k(x) \;=\; v \sum_{x \in \Upsilon_k} \bar{d}_k(x)\;, \tag{4}$$

where Υ_k is the set of all pixels in the detected FOV of channel k. In words, the support is determined by thresholding $\bar{d}_k$ at the value for which $(100 \times v)\%$ of the total energy in $\bar{d}_k$ is stored in pixels with intensities exceeding this threshold. The thresholding operation is depicted in Figure 2 for the case of a satellite with $m_v = 5$. Examples of images from the focal-plane channel are shown in Figure 2(a), and the shift-and-add image, $\bar{d}_1$, for $J = 64$ images is shown in Figure 2(b). We note that much of the noise observed in individual images is suppressed and that $\bar{d}_1$ is quite smooth with a fairly well-defined concentration of energy. The

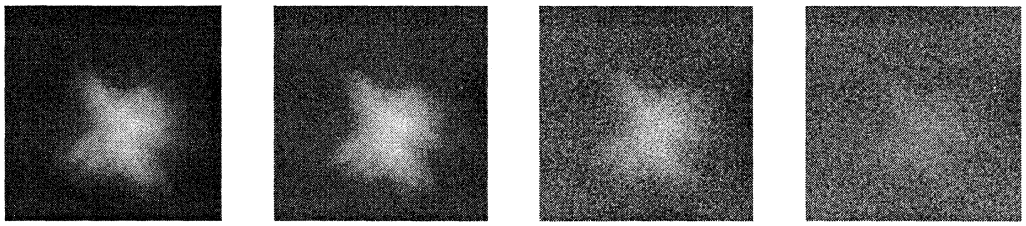

(a) (b) (c) (d)

Figure 3: Examples of simulated focal-plane images of a satellite with different values of visual magnitude, m_v. (a) $m_v = 4$ ($\bar{\mathcal{S}}_1 = 14.6$); (b) $m_v = 5$ ($\bar{\mathcal{S}}_1 = 8.2$); (c) $m_v = 6$ ($\bar{\mathcal{S}}_1 = 4.0$); (d) $m_v = 7$ ($\bar{\mathcal{S}}_1 = 1.8$).

support for a threshold corresponding to $\upsilon = 0.8$ is depicted with a binary mask in Figure 2(c), and we observe that $\Omega_1(0.8)$ encompasses the area of interest in $\bar{d}_1$. We have found experimentally that $\upsilon = 0.8$ specifies a satisfactory support for compact objects of interest.

Finally, we define the ensemble SNR as the spatially-averaged SNR over the support-limited, shift-and-add image:

$$\bar{\mathcal{S}}_k \equiv \sum_{x \in \Omega_k} \frac{\bar{d}_k(x)}{[\bar{d}_k(x) + \hat{\sigma}_n^2]^{\frac{1}{2}}}, \tag{5}$$

where the combined effects of dark-current and readout noise are represented with a single variance, $\hat{\sigma}_n^2$. If $b_d^k(x;\tau)$ and σ_r are known, then $\hat{\sigma}_n^2$ can be estimated from a spatial average of the variance at each pixel. This variance can also be estimated from the energy spectrum of the images by looking at the energy outside the diffraction limit of the system. The energy spectrum can be estimated with a standard periodogram technique [17]. Note that the estimate of the variance using energy measured outside the system passband is not immune to the influence of the signal-dependent noise in the imagery. The result is that $\hat{\sigma}_n^2$ is over-estimated when the signal from the image (and, hence, the variance of the signal-dependent noise) is much larger than the combined contribution of dark-current and readout noise. This over-estimation leads to under-estimation of $\bar{\mathcal{S}}_k$. As the signal from the image drops and the energy outside the system passband is dominated by dark-current and readout noise, $\hat{\sigma}_n^2$ becomes more accurate. It is usually the low-SNR cases that are of more interest, so we feel that it is acceptable to underestimate the SNR when it is large anyway. Examples of focal-plane images simulated for this study are shown Figures 3(a)-(d) for the cases of $m_v = 4$ ($\bar{\mathcal{S}}_1 = 14.6$), $m_v = 5$ ($\bar{\mathcal{S}}_1 = 8.2$), $m_v = 6$ ($\bar{\mathcal{S}}_1 = 4.0$), and $m_v = 7$ ($\bar{\mathcal{S}}_1 = 1.8$), respectively.

Performance Results

For this analysis, 64 image pairs were generated for $m_v = 4, 5, 6$, and 7. Reconstructions were made using $J = 64$, 32, and 16 phase-diverse image pairs. For the 32 image-pair analysis, a set of 64 images was arbitrarily divided into two disjoint subsets of 32 image pairs each. Similarly, four disjoint subsets were formed to perform the 16 image-pair analysis. Thus, a total of 7 reconstructions were formed (1 for $J = 64$, 2 for $J = 32$, and 4 for $J = 16$) for each value of m_v, for a total of 28 reconstructions. The standard reconstruction strategy employed in these simulations is to begin with a 90 Zernike-polynomial aberration parameterization to establish the low-order shape of the phase screens, and then to follow this with a discretized-pupil parameterization, in which the aberrations are described on a point-by-point basis across the telescope aperture. A regularizing, Gaussian sieve is used for all object estimates. The width is varied

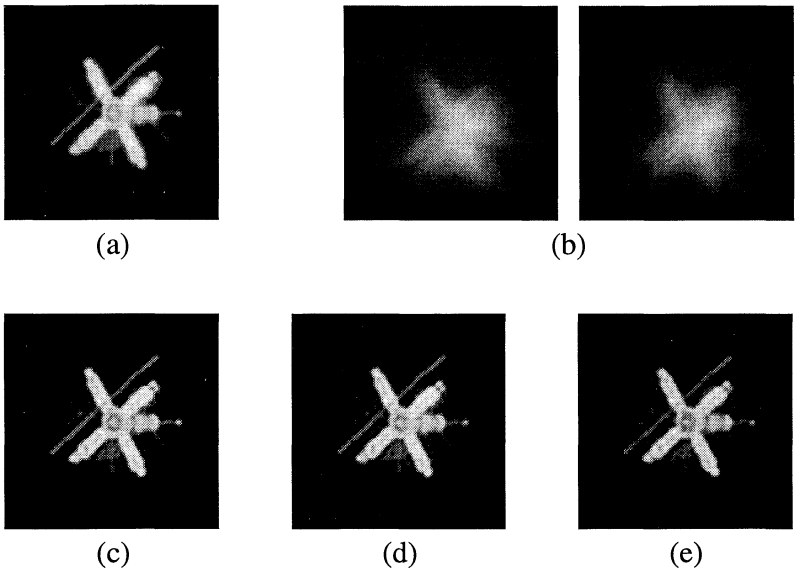

Figure 4: Results for a satellite with m_v=4 ($\bar{\mathcal{S}}_1 = 14.6$). (a) Noiseless, diffraction-limited image; (b) Example of a conventional (left) and diversity image; (c) 64 image-pair reconstruction; (d) Example of a 32 image-pair reconstruction; (e) Example of a 16 image-pair reconstruction.

depending on the SNR of the imagery. Typically, between 500 and 600 total iterations are performed, and an automatic stopping criterion based on the percent change in the log-likelihood function is employed.

Results for the most favorable case ($m_v = 4$, $\bar{\mathcal{S}}_1 = 14.6$) are shown in Figure 4. The diffraction-limited image is displayed in Figure 4(a) for reference, and example images in Figure 4(b) serve as visual aids to help gauge the SNR. In Figures 4(c), (d) and (e), respectively, we find the 64 image-pair, a 32 image-pair and a 16 image-pair reconstruction. In each case, the reconstruction is slightly sharper than the diffraction-limited image. Even the 16 image-pair reconstruction is quite good, and both the thin, diagonally-oriented feature (we'll refer to this as the *diagonal antenna*) and the thin, horizontal feature to the far right of the main body of the satellite (the *horizontal antenna*) are well-resolved.

The simulation experiments for each value of m_v are summarized in the array of reconstructions shown in Figure 5. The SNR is still fairly favorable ($\bar{\mathcal{S}}_1 = 8.2$) for $m_v = 5$, even though the detector noise is much more visible in the data [examples are shown in Figure 2(a)]. Nonetheless, we still find that the reconstructions [Figures 5(d)-(f)] are quite good in that the diagonal and horizontal antennae are recovered quite nicely. We do begin to notice a larger degree of pixel-to-pixel variation than observed for $m_v = 4$ [Figures 5(a)-(c)], particularly on the cylindrical satellite body to the left of the horizontal antenna. Whereas the gross intensity variation is recovered, we note that there are variations at a finer spatial scale. The eye tends to integrate over this variation, however, and the reconstructions are still highly interpretable. The 16 image-pair reconstruction in Figure 5(f) is beginning to show signs of degradation, particularly with respect to the support of the reconstruction. We begin to observe residual energy in a dim, speckle-like cloud surrounding the reconstruction. Nonetheless, we believe that an analyst would still find that a 16-realization reconstruction is satisfactory.

The SNR drops to 4.0 for $m_v = 6$ [see Figure 3(c)], and we begin to notice in Figures 5(h) and (i) that the reconstruction fidelity visually deteriorates for $J = 32$ and $J = 16$. For $m_v = 4$ and $m_v = 5$, a Gaussian-shaped smoothing sieve with a standard deviation of 1 pixel was used to regularize the reconstructions. The width of the sieve was broadened to 1.5 pixels for $m_v = 6$, and we observe a slight overall reduction in

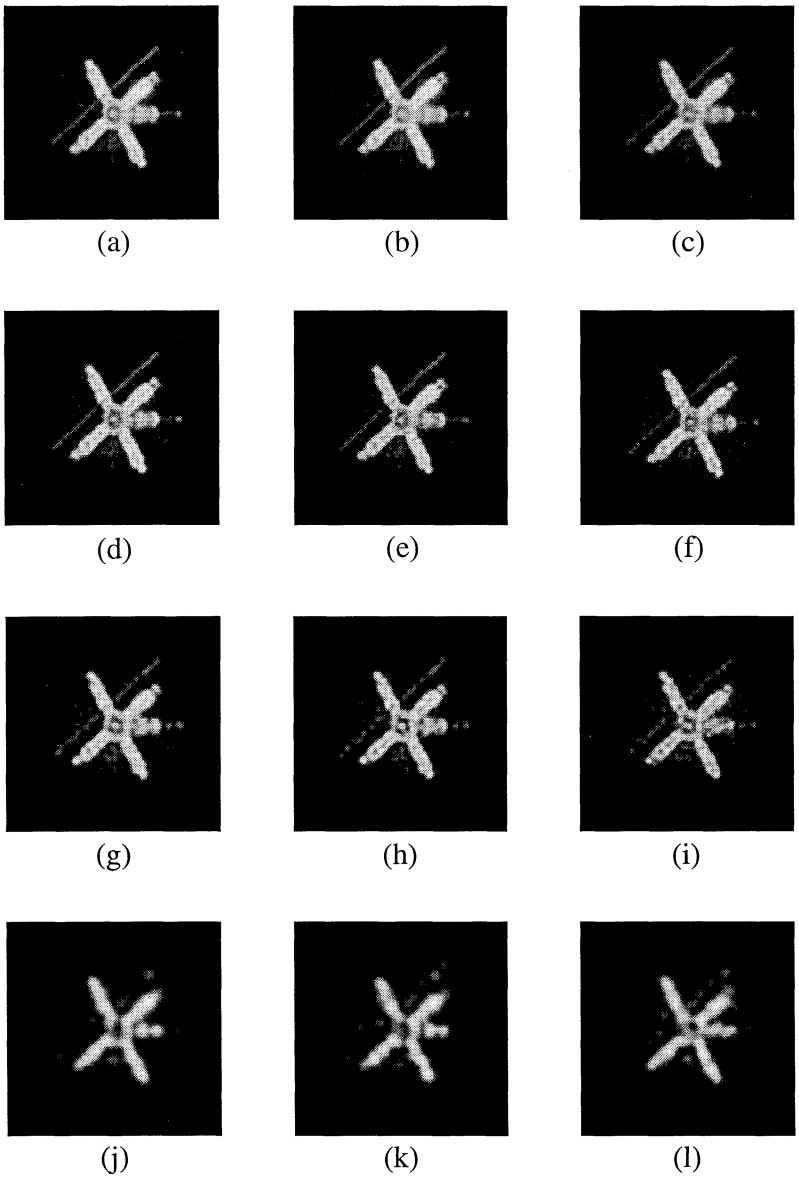

Figure 5: Summary of PDS simulations. (a) $J = 64$, $m_v = 4$, $\bar{\mathcal{S}}_1 = 14.6$; (b) $J = 32$, $m_v = 4$, $\bar{\mathcal{S}}_1 = 14.6$; (c) $J = 16$, $m_v = 4$, $\bar{\mathcal{S}}_1 = 14.6$; (d) $J = 64$, $m_v = 5$, $\bar{\mathcal{S}}_1 = 8.2$; (e) $J = 32$, $m_v = 5$, $\bar{\mathcal{S}}_1 = 8.2$; (f) $J = 16$, $m_v = 5$, $\bar{\mathcal{S}}_1 = 8.2$; (g) $J = 64$, $m_v = 6$, $\bar{\mathcal{S}}_1 = 4.0$; (h) $J = 32$, $m_v = 6$, $\bar{\mathcal{S}}_1 = 4.0$; (i) $J = 16$, $m_v = 6$, $\bar{\mathcal{S}}_1 = 4.0$; (j) $J = 64$, $m_v = 7$, $\bar{\mathcal{S}}_1 = 1.8$; (k) $J = 32$, $m_v = 7$, $\bar{\mathcal{S}}_1 = 1.8$; (l) $J = 16$, $m_v = 7$, $\bar{\mathcal{S}}_1 = 1.8$.

sharpness with respect to previous reconstructions. Another characteristic of these reconstructions can be observed in the diagonal and horizontal antennae. These linear, low-SNR features develop gaps, breaking up along their length. The support of the 16 image-pair reconstruction is less well-defined, and the speckle-like artifacts surrounding the body of the satellite are as bright as the horizontal antenna feature in some areas. The fact that the reconstructed antennae pixels align themselves linearly helps one distinguish these from artifacts. Since the antennae are about 1/2 the intensity of the brightest portions of the satellite, the SNR is lower than 4.0 for these pixels, and it is impressive that these features are restored at all.

Finally, the last case explored is when $m_v = 7$ and $\bar{\mathcal{S}}_1 = 1.8$. We found through various reconstruction experiments that a sieve with a width of 3 pixels yielded the most interpretable results. The reconstructions, shown in Figures 5(j)-(l), do not exhibit many fine-resolution internal features, and the support is somewhat eroded. This erosion can be understood when the effect of blurring is considered. The blurred edges in the raw imagery are lost in the noise [see Figure 3(d)], so the net result is an estimate of the object support that eats into these edges. We find that the erosion of the support in very low SNR regimes is a common feature of deblurring algorithms. While even the best reconstruction for the case of $J = 64$ is still quite poor with respect to the diffraction-limited image, an image analyst could surely learn something from the reconstruction in Figure 5(j) that cannot be observed in the extremely noisy raw imagery. We conclude that 16 realizations are adequate for $m_v = 4$ and $m_v = 5$, but that 32 realizations or more are desired for $m_v = 6$, where the SNR is 4.0 and the performance is just beginning to decline. There is a large jump in loss of fidelity between $m_v = 6$ and $m_v = 7$, where the SNR dips below 2.0. In general, using 32 image pairs is sufficient, and it does not appear that a significant improvement in fidelity is obtained when using 64 image pairs, which roughly doubles the computations per reconstruction.

3. SATELLITE RECONSTRUCTIONS FROM REAL DATA

Images of satellites were collected with the 1.5-meter telescope at the SOR using adaptive-optics (AO) compensation. The image data were collected at a center wavelength of 0.85 μm with a full-width at half-maximum optical bandwidth of about 0.1 μm. The selected satellites were small enough to accommodate the use of a single camera, so *both* the conventional and the diversity channels were imaged onto separate sides of a 12-bit, 64×64 CCD array. The signal was divided into two channels with a polarizing beamsplitter, and two BK7 glass plates with 1/8-inch and 1/4-inch thickness, respectively, were inserted into one channel to introduce a quadratic phase diversity of 0.7 wave peak-to-valley. The data are approximately Nyquist sampled at 283 $nrad$ per pixel. Thus, the entire CCD captures a $18\mu rad \times 18\mu rad$ FOV, which limits the satellite subtense when the two channels do not interfere. An important aspect of the PDS reconstruction algorithm is the accurate modeling of the imaging system, and calibration data were used to characterize the noise properties of the CCD (dark current and readout noise). Each of about a dozen satellite passes imaged consists of short-exposure images taken in sets of 256 frames for exposures times of 2, 5 or 10 $msec$. Sets of 256 dark frames (shutter closed) taken at the same exposure setting typically were collected after each set of data.

The results of reconstructing a pass of Catalog No. (CATNO) 4419, which was imaged with self-referenced AO compensation, is discussed here. About a dozen, 256-frame image sets of varying SNR were collected across the pass. Examples of 5-$msec$ image pairs (conventional on top) from the set with the largest SNR are shown in Figure 6(a). In this case, $\bar{\mathcal{S}}_1 = 7.4$, which is quite comparable to the simulated case of $m_v = 5$. We observe that the two images on the left of Figure 6(a) are reasonably well compensated, with aberrations that are quite a bit milder than a typical realization of Kolmogorov turbulence used in the simulations. The other two image pairs shown are examples of average and poor compensation, respectively, demonstrating our introductory assertion that aberrations can still be appreciable in systems employing AO

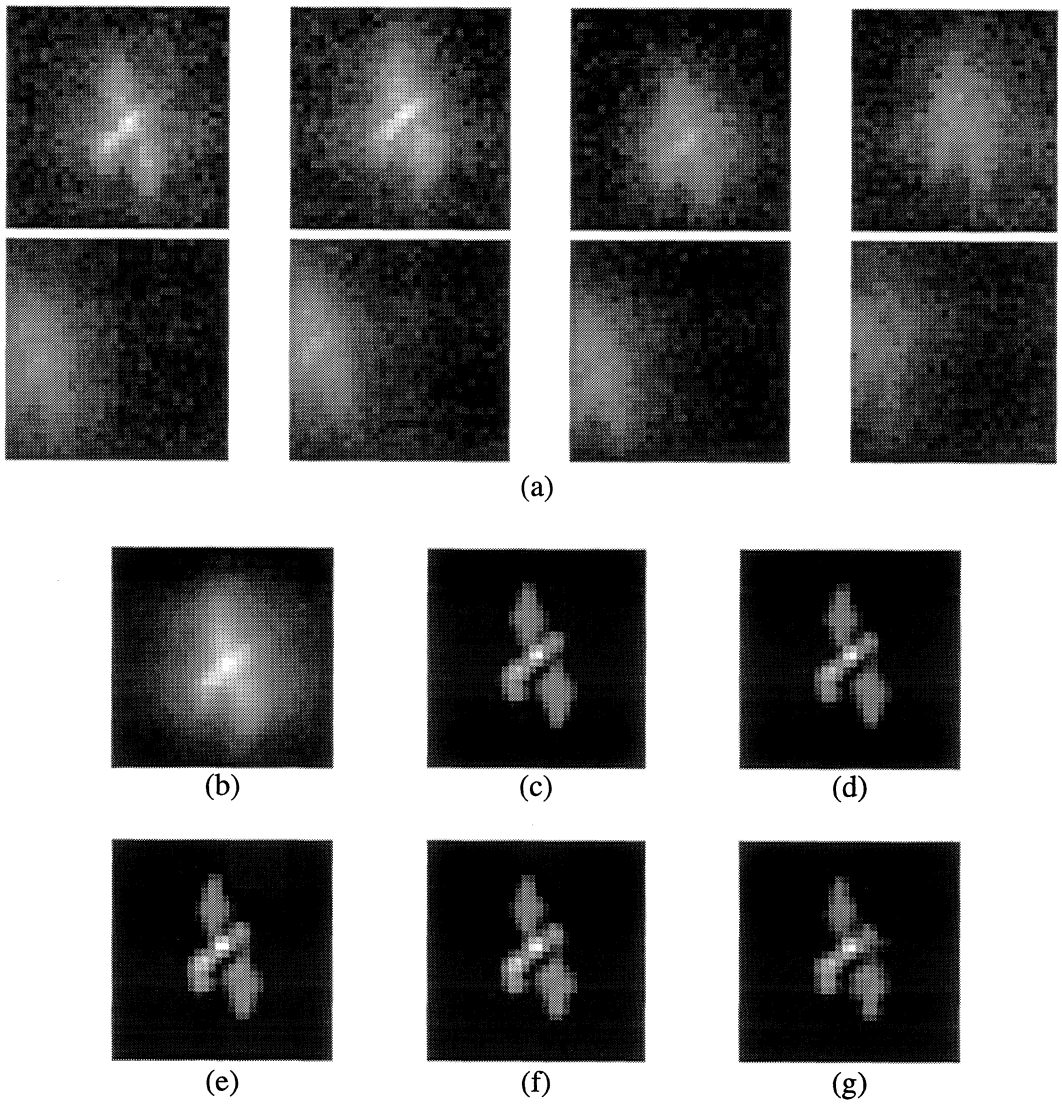

Figure 6: PDS reconstructions of Catalog No. 4419. The set of 256 image pairs was divided into disjoint subsets of $256/J$ image pairs each, for $J = 64$, 32, 24, 16 and 8. (a) Examples of conventional (top) and diversity image pairs for a range of AO compensation quality. The ensemble SNR in the conventional channel is $\bar{\mathcal{S}}_1 = 7.4$; (b) A 64-pair shift-and-add image; (c) Example of a 64-pair restoration; (d) Example of a 32-pair restoration; (e) Example of a 24-pair restoration; (f) Example of a 16-pair restoration; (g) Example of an 8-pair restoration.

correction. We note that a portion of the diversity images fall outside of the detector FOV. Fortunately, the PDS algorithm is designed to handle this using a processing "guard band" that is particularly important for applications of imaging scenes that extend beyond the sensor FOV [7]. We also note that the images translate somewhat from frame to frame; PDS naturally registers the data estimating wavefront tilt and, therefore, does not require that the data be aligned prior to processing.

The consistency of PDS object estimates with respect to the number of image pairs input to the algorithm is summarized in Figure 6. For each number of images pairs, J, the 256-pair set was divided into $256/J$ (truncated to the nearest integer) disjoint subsets, and a restoration was made for each subset. The 64-realization shift-and-add image, $\bar{d}_1(x)$, that is used as the initial guess to one of the four 64-pair subsets is shown in Figure 6(b). The corresponding 64-pair restoration is shown in Figure 6(c). This restoration has an excellent support estimate and interesting intensity variations. A glint on the main body is observed, and shadowing is noted at the junction of the main body with the solar panels. The shadowing is consistent with our intuition and experience with sun-illuminated artificial satellites. There is also an interesting feature at the base of the main body that protrudes roughly vertically. Representative restorations for the cases of $J = 32$, 24, 16 and 8 image pairs are found in Figures 6(d)-(g), respectively. There is a high degree of consistency between the restorations, and it is not until we use only $J = 8$ image pairs that the intensity features begin to vary and the support is less defined. Nonetheless, this restoration improves dramatically upon any individual short-exposure image and is significantly sharper than the shift-and-add initial estimate. This group of restorations also demonstrates that PDS can work well on images with favorable SNR, even when a portion of the diversity image data fall outside of the FOV. Furthermore, high-fidelity restorations can be obtained with only 16 image pairs, and decent performance is exhibited here with as few as only 8 pairs. Fine-resolution PDS restoration of solar granulation have been made using only 5 image pairs [7, 8], but the satellite-imaging results presented here are from a more stressing regime of operation with respect to SNR.

A powerful means for assessing reconstruction accuracy is the comparison of restorations at different points in the satellite pass. The CATNO 4419 pass provides us with a very nice time sequence of 12 restorations that shows the satellite at a variety of aspects. The sequence of restorations using $J = 32$ image pairs is shown in Figure 7. The first 9 sets were collected with a 5 *msec* exposure, and the last 3 sets use 2 *msec*. The SNR, $\bar{\mathcal{S}}_1$, has an average value of 6.0 for the 5 *msec* sets and only 2.2 for the 2 *msec* data. The time interval between sets is not evenly spaced, and our best estimate (based on the time spent above 45 degrees elevation) is approximately 10 seconds between restorations. The third restoration in the sequence was shown previously in Figure 6(d). The restorations share many common features. Perhaps most meaningful of all is the fact that these features evolve with the change in satellite aspect in a believable fashion. For instance, (1) a glint on the main body begins to form in restoration frame 2 and persists for several frames before fading out; (2) shadowing of the panels near the main body is common to most of the restorations; (3) the main body gradually experiences a foreshortening with aspect; (4) a subtle, low-intensity region on the panels is observed in frames 4-7. These are just a few of the characteristics that persist throughout the pass. One image analyst also noted that the two panels are not fully planar, and that they retain a slight zigzag from deployment. The value of a time series of restorations like this should not be underestimated, and has already provided a third dimension of information for astronomers studying the evolution of small-scale solar features from ground-based observatories [12]. The reduction of artifacts and the ability to view the object at a variety of angles opens the door to a wealth of reliable information that can be mined from movies of satellites.

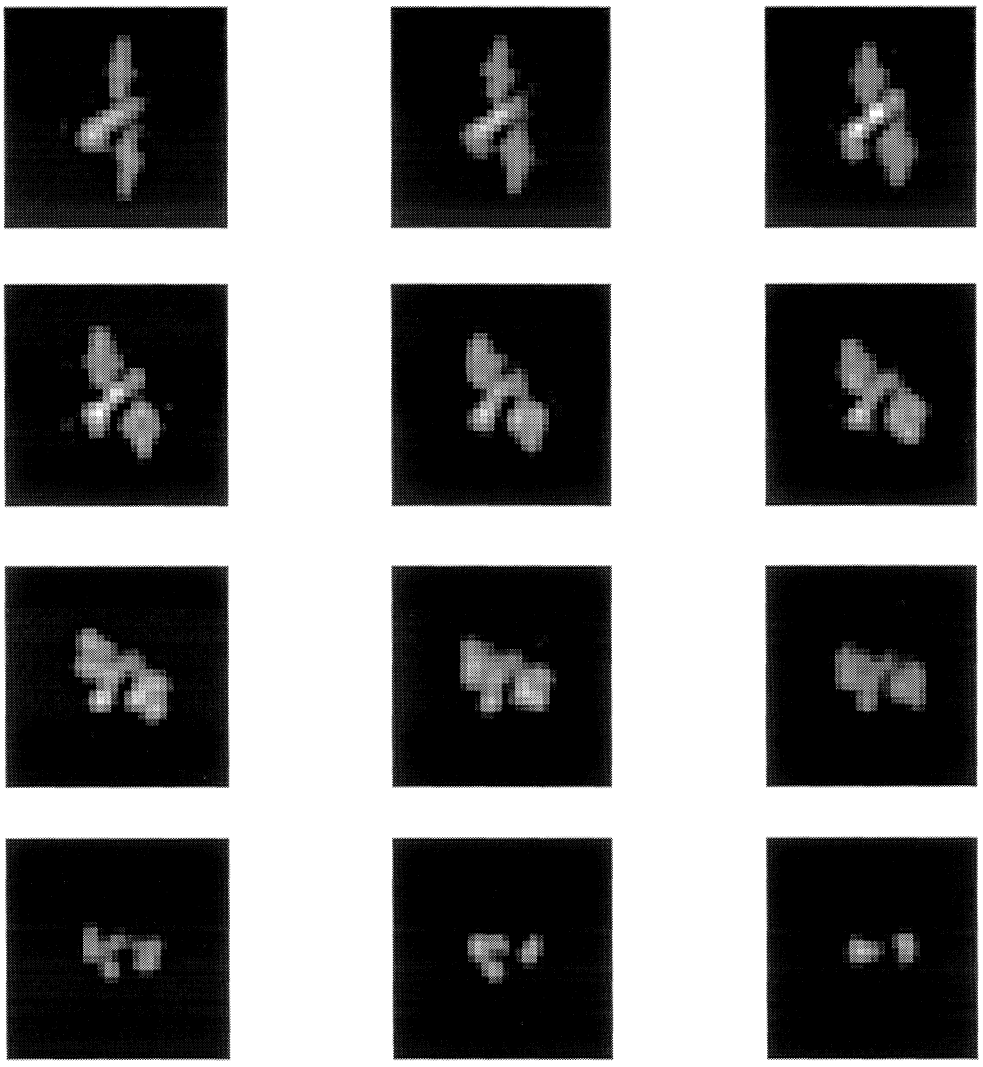

Figure 7: Time series of Catalog No. 4419 restorations. Each restoration derives from 32 image pairs. The sequence rasters from the upper left to the bottom right. The first 9 sets derive from data collected with a 5 *msec* exposure, and the last three were collected with a 2 *msec* exposure. The average conventional-channel SNR is 6.0 for the 5 *msec* data and 2.2 for the 2 *msec* data.

4. CONCLUSIONS

The use of PDS for satellite reconstruction was demonstrated in simulation for a variety of SNR's. For a given turbulence strength, satellite reconstruction fidelity was evaluated as a function of quality and quantity of data. We found that performance degrades as expected as both the SNR and number of image pairs are reduced. The credibility of this study is enhanced by reconstructions from compensated data collected with the 1.5-meter telescope at the SOR. The authenticity of the reconstuctions was enhanced via a time series of reconstructions for CATNO 4419. We confirmed the simulation findings when we showed that excellent reconstructions can be obtained with 16 image pairs when the SNR is high. Important features persist throughout the pass, and changes in aspect and the location of shadows evolve as expected. Glints evolve rapidly as expected, and the size and shape of the satellite varies in a believable fashion. In addition, details of the restorations were corroborated with sketches of the actual objects, and features such as the orientation of solar panels were identified by analysts experienced in space-object imaging.

ACKNOWLEDGEMENTS

We acknowledge the efforts of Cassandra Hoye and Sean Frazier of ERIM International, who conducted much of the simulation and real-data computer processing. We also thank Byron Welsh of the Air Force Institute of Technology and Michael Roggemann of the Michigan Technological Institute for providing the simulated satellite rendering and phase aberrations. Finally, we thank Richard Rast of the SOR for providing satellite collection planning and expertise in space-object identification. This research was supported by the U.S. Air Force Phillips Laboratory under two separate contracts. Computing resources for the simulation investigation were provided by the Maui High Performance Computing Center (MHPCC) in conjunction with the AMOS/MHPCC Research and Development Consortium.

References

[1] A. Labeyrie. Attainment of diffraction limited resolution in large telescopes by fourier analysing speckle patterns in star images. *Astron. and Astrophys.*, 6:85–87, 1970.

[2] J. C. Dainty. Stellar speckle imaging. In *Topics in Applied Physics: Laser Speckle and Related Phenomena, 2nd edition, J. C. Dainty, editor*, pages 297–328. Springer-Verlag, New York, 1984.

[3] J. Primot, G. Rousset, and J. C. Fontanella. Deconvolution from wave-front sensing: a new technique for compensating turbulence-degraded images. *J. Opt. Soc. Am.*, 7:1598–1608, 1990.

[4] J. D. Gonglewski, D. G. Voelz, D. C. Dayton J. S. Fender, B. K. Spielbusch, and R. E. Pierson. First astronomical application of postdetection turbulence compensation: images of α aurigae, ν ursae majoris, and α geminorum using self-referenced speckle holography. *Appl. Opt.*, 29:4527–4529, 1990.

[5] R. G. Paxman, T. J. Schulz, and J. R. Fienup. Phase-diverse speckle interferometry. In *Signal Recovery and Synthesis IV*, Technical Digest Series 11, (OSA) New Orleans, LA, April 1992.

[6] R. G. Paxman and J. H. Seldin. Fine-resolution imaging of solar features using phase-diverse speckle imaging. In *Real Time and Post-Facto Solar Image Correction*, 13th Sacramento Peak Summer Workshop, Sunspot NM, September 1992.

[7] J. H. Seldin and R. G. Paxman. Phase-diverse speckle reconstruction of solar data. In *Proc. of the SPIE Conf. on Image Applications and Restoration* **2302**, *T. J. Schulz and D. L. Snyder, eds.*, pages 268–280, San Diego, CA, July 1994.

[8] R. G. Paxman, J. H. Seldin, M. G. Löfdahl, G. B. Scharmer, and C. U. Keller. Evaluation of phase-diversity techniques for solar-image restoration. *Astrophysical Journal*, 467, 1996.

[9] R. A. Gonsalves and R. Chidlaw. Wavefront sensing by phase retrieval. In *Proc. of the SPIE Conf. on Applications of Digtial Image Processing III* **207**, *A. G. Tescher, ed.*, pages 32–39, San Diego, CA, 1979.

[10] R. G. Paxman and J. R. Fienup. Optical misalignment sensing and image reconstruction using phase diversity. *J. Opt. Soc. Am.*, 5:914–923, 1988.

[11] R. G. Paxman, T. J. Schulz, and J. R. Fienup. Joint estimation of object and aberrations by using phase diversity. *J. Opt. Soc. Am.*, 9:1072–1085, 1992.

[12] J. H. Seldin, R. G. Paxman, and C. U. Keller. Time series restoration from ground-based solar observations. In *Missions to the Sun, Proceedings of the SPIE* **2804-29**, Denver, Colorado, August 1996.

[13] J. H. Seldin, R. G. Paxman, and B. L. Ellerbroek. Post-detection correction of compensated imagery using phase-diverse speckle. In *Proc. of ESO/OSA Topical Meeting on Adaptive Optics, M. Cullum, ed.*, Garching, Germany, 1995.

[14] R. J. Noll. Zernike polynomials and atmospheric turbulence. *J. Opt. Soc. Am.*, 66:207–211, 1976.

[15] D. L. Snyder and M. I. Miller. The use of sieves to stabilize images produced with the EM algorithm for emission tomography. *IEEE Trans. Nuclear Science*, NS-32:3864–3872, 1985.

[16] J. S. Accetta and D. L. Schumaker (executive editors). *The Infrared & electro-optical systems handbook.* Infrared Information Analysis Center (ERIM, Ann Arbor, Michigan) and SPIE Optical Engineering Press (Bellingham, Washington), 1993.

[17] S. L. Marple Jr. *Digital Spectral Analysis.* Prentice-Hall, Englewood-Cliffs N.J., 1987.